AERODYNAMICS OF AIRFOILS AT LOW REYNOLDS NUMBERS

Dan Mateescu, dan.mateescu@mcgill.ca
McGill University, Montreal, QC, Canada H3A 2K6

Abstract. *A special interest has recently been devoted to the aerodynamics of airfoils at low and very low Reynolds numbers. This interest is driven by a variety of applications ranging from domestic windmills to unmanned* aerial *vehicles (UAV) and* micro-air-vehicles (MAV), *which were made possible by the recent advances in micro-electro-mechanical systems (MEMS). The flows past airfoils at low Reynolds numbers are dominated by viscous effects and flow separation phenomena, which complicate the understanding of airfoil aerodynamics in these conditions. The aim of this paper is to present the special features of the aerodynamic characteristics of airfoils at very low Reynolds numbers. These are obtained with an efficient numerical analysis based on a pseudo-time integration method using artificial compressibility to accurately solve the Navier-Stokes equations; this method represents an extension of the method developed by Mateescu & Venditti (2001) for the analysis of the unsteady confined flows with oscillating boundaries and with multiple separation regions. The flow problem is solved in this method in a rectangular computational domain obtained by a coordinate transformation from the physical flow domain around the airfoil at incidence. This method, which does not require a lengthy grid generation procedure, uses a central differencing approach on a stretched staggered grid in the computational domain. A special decoupling procedure using the continuity equation reduces the problem to the solution of scalar tridiagonal systems of equations, which enhances substantially the computational efficiency of the method. This method has been used to obtain the pressure distribution, lift and drag coefficients for several NACA airfoils at various incidences and low Reynolds numbers between 400 and 6000. The obtained airfoil solutions are successfully validated by comparison with the numerical results obtained by Kunz & Kroo (2000) for Reynolds numbers between 1000 and 6000 (no results were available for Reynolds numbers smaller than 1000). This paper presents a detailed study of the influence of the Reynolds number, angle of attack and airfoil relative thickness and camber on the pressure distribution, lift and drag coefficients. The variation of the lift and drag coefficients with the angle of attack is presented for several airfoils in various flow conditions. In order to better understand the complex flow separation phenomena in the viscous flows past airfoils at very low Reynolds numbers, the onset of separation and reattachment positions, as well as the flow separation length, have also been calculated, analyzing the effect of various parameters (Reynolds number, angle of attack, relative thickness and camber, and the maximum camber position along the chord) affecting the flow separation. The streamline contours for the flow with separations past several airfoils at various Reynolds numbers and angles of attack have also been generated and compared.*

Keywords: *Low Reynolds number flows, Airfoil aerodynamics, Subsonic flows, Viscous flows*

1. INTRODUCTION

A special interest has recently been devoted to the aerodynamics of airfoils at low and very low Reynolds numbers. This interest is driven by a variety of applications ranging from domestic windmills to special military aircraft and unmanned aerial vehicles (UAV), which were made possible by the recent advances in the micro-electro-mechanical systems (MEMS). Very small aircrafts called micro-air-vehicles (MAV) can operate in various environments including tunnels, desert and jungle. These applications have shown that many questions are unanswered regarding the airfoil aerodynamics at low and very low Reynolds numbers. The flows past airfoils at low Reynolds numbers are dominated by viscous effects and flow separation phenomena, which complicate the understanding of airfoil aerodynamics in these conditions.

The aim of this paper is to present the special features of the aerodynamic characteristics of airfoils in incompressible flows at very low Reynolds numbers, which are obtained with an efficient numerical analysis based on a pseudo-time integration method using artificial compressibility to solve accurately the Navier-Stokes equations. This method represents an extension of the method developed by Mateescu & Venditti (2001) for the analysis of the unsteady confined flows with oscillating boundaries and with multiple separation regions. The flow problem is solved in this method in a rectangular computational domain obtained by a coordinate transformation from the physical flow domain around the airfoil at incidence.

This method does not require a lengthy grid generation procedure and uses a central differencing approach on a stretched staggered grid (which avoids the odd-and-even points decoupling) in the computational domain. The method employs a special decoupling procedure using the continuity equation in order to reduce the problem to the solution of scalar tridiagonal systems of equations, which enhances substantially the computational efficiency of the method.

2. METHOD OF SOLUTION

Consider a cambered airfoil of chord c placed at an incidence α in a uniform stream of velocity U_∞, as shown in Figure 1. The viscous fluid flow past the airfoil is referred to a Cartesian reference system of coordinates cx, cy, where x and y are nondimensional coordinates, with the *x*-axis along the airfoil chord and its origin at the airfoil leading edge. Let $U_\infty u$ and $U_\infty v$ denote the fluid velocity components along the *x*- and *y*-axes, where u and v are the nondimensional velocity components. The airfoil upper and lower surfaces are defined by the equations

$$y = e_1(x) = h(x) + e(x) \ , \quad \text{and} \quad y = -e_2(x) = h(x) - e(x) \ , \tag{1}$$

where the subscripts 1 and 2 refer to the upper and lower surfaces, and where $h(x)$ and $e(x)$ define, respectively, the camberline and airfoil thickness variation along the airfoil chord. The special case of symmetric airfoils is characterized by $e_1(x) = e_2(x) = e(x)$ and $h(x) = 0$.

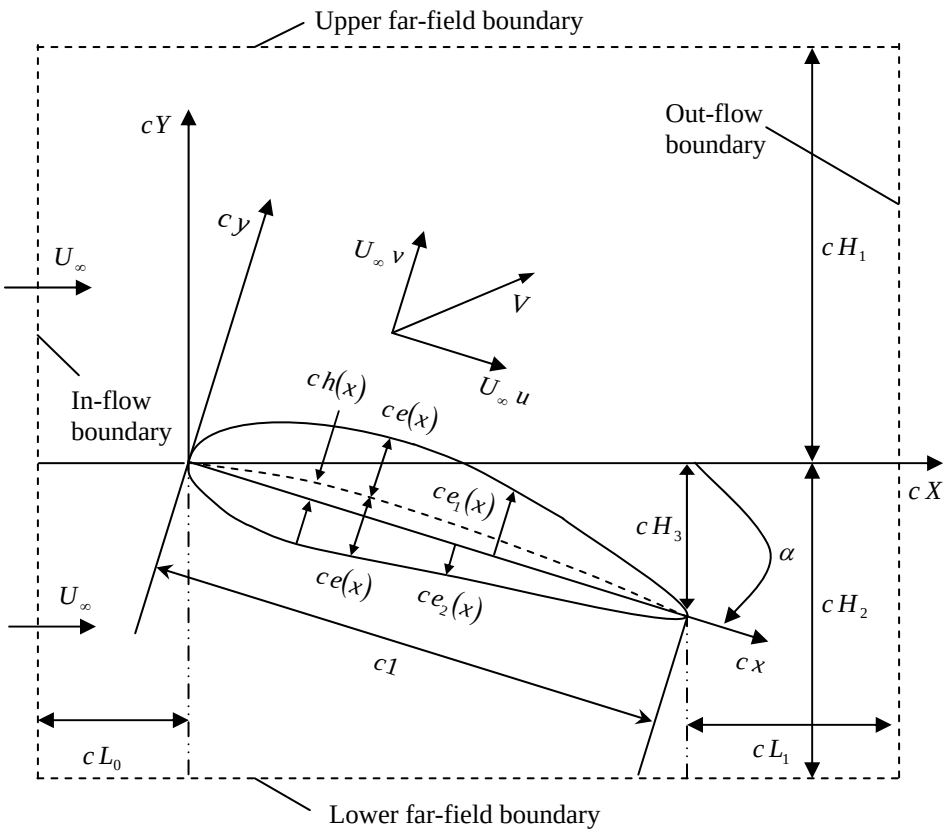

Figure 1. Geometry of a cambered airfoil in a uniform flow at incidence

The Navier-Stokes and continuity equations for the incompressible flow past the airfoil can be expressed in nondimensional conservation form as

$$\frac{\partial \mathbf{V}}{\partial \mathbf{t}} + \mathbf{Q}(\mathbf{V}, p) = \mathbf{0} \ , \qquad \nabla \bullet \mathbf{V} = \frac{\partial u}{\partial x} + \frac{\partial v}{\partial y} = 0 \ , \tag{2}$$

where $\mathbf{V} = \{u, v\}^{\mathrm{T}}$ represents the vector of the dimensionless velocity components and $\mathbf{Q}(\mathbf{V}, p)$, which includes the convective derivative, pressure and viscous terms, can be expressed in 2-D Cartesian coordinates in the form

$$\mathbf{Q}(\mathbf{V}, p) = \{Q_u(u, v, p), Q_v(u, v, p)\}^{\mathrm{T}} \ , \tag{3}$$

$$Q_u(u, v, p) = \frac{\partial (uu)}{\partial x} + \frac{\partial (vu)}{\partial y} + \frac{\partial p}{\partial x} - \frac{1}{\mathrm{Re}}\left(\frac{\partial^2 u}{\partial x^2} + \frac{\partial^2 u}{\partial y^2}\right) , \tag{4a}$$

$$Q_v(u, v, p) = \frac{\partial (uv)}{\partial x} + \frac{\partial (vv)}{\partial y} + \frac{\partial p}{\partial y} - \frac{1}{\mathrm{Re}}\left(\frac{\partial^2 v}{\partial x^2} + \frac{\partial^2 v}{\partial y^2}\right) , \tag{4b}$$

where p is the dimensionless pressure, nondimensionalized with respect to $\rho U_\infty{}^2$, and $\mathrm{Re} = cU_\infty / \nu$ is the Reynolds number based on the chord length (ρ and ν are the fluid density and kinematic viscosity). In the present

computational analysis we focus our attention on flows at low Reynolds numbers, in which the viscous effects play a very important role. For steady flows, $\partial \mathbf{V}/\partial t = 0$ in (2).

The problem is solved in a rectangular computational domain with 5 sub-domains which is obtained by the geometrical transformation

$$X = x\cos\alpha + y\sin\alpha \ , \qquad Y = f(x,y) \ , \tag{5}$$

where

$$f(x,y) = \begin{cases} -x\sin\alpha + y\cos\alpha & \text{for } x<0 \\ \dfrac{[y-e_1(x)]\cos\alpha}{H_1 - [-x\sin\alpha + e_1(x)\cos\alpha]}\,H_1 & \text{for } 0<x<1 \text{ and } y>e_1(x) \\ \dfrac{[y+e_2(x)]\cos\alpha}{H_2 + [-x\sin\alpha - e_2(x)\cos\alpha]}\,H_2 & \text{for } 0<x<1 \text{ and } y<-e_2(x) \\ \dfrac{H_3 + (-x\sin\alpha + y\cos\alpha)}{H_1+H_3}\,H_1 & \text{for } x>1 \text{ and } y>-H_3 \\ -H_2\dfrac{H_3 + (-x\sin\alpha + y\cos\alpha)}{-H_2+H_3} & \text{for } x>1 \text{ and } y<-H_3 \end{cases} \ , \tag{6}$$

in which H_1 and H_2 are the nondimensional physical coordinates of the upper and lower boundaries of the computational domain (as shown in Fig. 1), and $H_3 = \sin\alpha$. The upstream inflow and downstream outflow boundaries of the computational domain are defined by the nondimensional coordinates $X = -L_0$ and $X = L_1 + \cos\alpha$.

In the computational domain obtained by this coordinate transformation, the steady Navier-Stokes and continuity equations become

$$\mathbf{G}(\mathbf{V},p) = \mathbf{0} \ , \qquad \mathbf{D}\,\mathbf{V} = 0 \ , \tag{7}$$

where

$$\mathbf{D}\,\mathbf{V} = C_7\frac{\partial u}{\partial X} + C_2\frac{\partial u}{\partial Y} + C_8\frac{\partial v}{\partial X} + C_3\frac{\partial v}{\partial Y} \ , \tag{8}$$

$$\mathbf{G}(\mathbf{V},p) = \{G_u(u,v,p),\, G_v(u,v,p)\}^{\mathrm{T}} \tag{9}$$

$$G_u(u,v,p) = C_7\frac{\partial(uu)}{\partial X} + C_2\frac{\partial(uu)}{\partial Y} + C_8\frac{\partial(vu)}{\partial X} + C_3\frac{\partial(vu)}{\partial Y} + C_7\frac{\partial p}{\partial X} + C_2\frac{\partial p}{\partial Y} + C_1\frac{\partial^2 u}{\partial X^2} + C_6\frac{\partial^2 u}{\partial X\,\partial Y} + C_5\frac{\partial^2 u}{\partial Y^2} + C_4\frac{\partial u}{\partial Y} \ , \tag{10a}$$

$$G_v(u,v,p) = C_8\frac{\partial(vv)}{\partial X} + C_3\frac{\partial(vv)}{\partial Y} + C_7\frac{\partial(uv)}{\partial X} + C_2\frac{\partial(uv)}{\partial Y} + C_8\frac{\partial p}{\partial X} + C_3\frac{\partial p}{\partial Y} + C_1\frac{\partial^2 v}{\partial X^2} + C_6\frac{\partial^2 v}{\partial X\,\partial Y} + C_5\frac{\partial^2 v}{\partial Y^2} + C_4\frac{\partial v}{\partial Y} \ , \tag{10b}$$

in which

$$C_1 = -\frac{1}{\mathrm{Re}} \ , \quad C_2 = \frac{\partial f}{\partial x} \ , \quad C_3 = \frac{\partial f}{\partial y} \ , \quad C_4 = -\frac{1}{\mathrm{Re}}\left(\frac{\partial^2 f}{\partial x^2} + \frac{\partial^2 f}{\partial y^2}\right) , \tag{11a}$$

$$C_5 = -\frac{1}{\mathrm{Re}}\left[\left(\frac{\partial f}{\partial x}\right)^2 + \left(\frac{\partial f}{\partial y}\right)^2\right] , \quad C_6 = -\frac{2}{\mathrm{Re}}\left[\cos\alpha\,\frac{\partial f}{\partial x} + \sin\alpha\,\frac{\partial f}{\partial y}\right] , \quad C_7 = \cos\alpha \ , \quad C_8 = \sin\alpha \ . \tag{11b}$$

This steady incompressible flow problem is then solved with an iterative pseudo-time relaxation procedure using artificially-added compressibility, by augmenting the continuity and Navier-Stokes equations with pseudo-time derivative terms involving pressure and velocity (Chorin 1984) in the form

$$\delta\frac{\partial p}{\partial t} + \mathbf{D}\mathbf{V} = \mathbf{0} \ , \qquad \frac{\partial \mathbf{V}}{\partial t} + \mathbf{G}(\mathbf{V},p) = \mathbf{0} \ , \tag{12}$$

where δ represents the coefficient of artificially-added compressibility. Various authors proposed different methods to determine the value of this artificial compressibility, but optimal values of δ are better obtained by numerical experimentation. In this work, an initial optimum value for δ is determined based on the theory of characteristics (Mateescu *et al*. 1994a, b, 2001) and then is modified by numerical experimentation.

The pseudo-continuity and Navier-Stokes equations (12) are solved in pseudo-time until a steady state is reached and the physical divergence-free condition (corresponding to the steady-state continuity equation) is satisfied. An implicit Euler scheme is used in this respect to discretize these equations in pseudo-time between the pseudo-time levels t^n and t^{n+1} in the form

$$\frac{\mathbf{V}^{n+1}-\mathbf{V}^n}{\Delta t}+\mathbf{G}^{n+1}(\mathbf{V},p)=\mathbf{0}\ , \qquad \frac{p^{n+1}-p^n}{\Delta t}+\frac{1}{\delta}\ \mathbf{D}\mathbf{V}^{n+1}=0\ , \tag{13}$$

where $\Delta t = t^{n+1}-t^n$. These equations are expressed in terms of the pseudo-time variations $\Delta u = u^{n+1}-u^n$, $\Delta v = v^{n+1}-v^n$, $\Delta p = p^{n+1}-p^n$, in the matrix form

$$\left[\mathbf{I}+\Delta t\left(\mathbf{D}_X+\mathbf{D}_Y\right)\right]\Delta\mathbf{f}=\Delta t\ \mathbf{S}\ , \tag{14}$$

where $\Delta\mathbf{f}=\left[\Delta u,\Delta v,\Delta p\right]^{\mathrm{T}}$, $\mathbf{I}$ is the identity matrix, and

$$\mathbf{D}_X=\begin{bmatrix} M & 0 & C_7\dfrac{\partial}{\partial X} \\ 0 & M & C_8\dfrac{\partial}{\partial X} \\ \dfrac{C_7}{\delta}\dfrac{\partial}{\partial X} & \dfrac{C_8}{\delta}\dfrac{\partial}{\partial X} & 0 \end{bmatrix}, \quad \mathbf{D}_Y=\begin{bmatrix} N & 0 & C_2\dfrac{\partial}{\partial Y} \\ 0 & N & C_3\dfrac{\partial}{\partial Y} \\ \dfrac{C_2}{\delta}\dfrac{\partial}{\partial Y} & \dfrac{C_3}{\delta}\dfrac{\partial}{\partial Y} & 0 \end{bmatrix}, \quad \mathbf{S}=\begin{bmatrix} -G_u\left(u^n,v^n,p^n\right) \\ -G_v\left(u^n,v^n,p^n\right) \\ -\left(1/\delta\right)\mathbf{D}\mathbf{V}^n \end{bmatrix}, \tag{15}$$

in which the differential operators M and N are defined as

$$M\phi=C_7\frac{\partial\left(u^n\phi\right)}{\partial X}+C_8\frac{\partial\left(v^n\phi\right)}{\partial X}+C_1\frac{\partial^2\phi}{\partial X^2}\ , \qquad N\phi=C_2\frac{\partial\left(u^n\phi\right)}{\partial Y}+C_3\frac{\partial\left(v^n\phi\right)}{\partial Y}+C_6\frac{\partial^2\phi}{\partial X\,\partial Y}+C_5\frac{\partial^2\phi}{\partial Y^2}+C_4\frac{\partial\phi}{\partial Y}\ , \tag{16}$$

A factored Alternate Direction Implicit (ADI) scheme is then used to separate equation (14) into two successive sweeps in x and y, defined by the equations

$$\left[\mathbf{I}+\Delta t\,\mathbf{D}_Y\right]\Delta\mathbf{f}^*=\Delta t\ \mathbf{S}\ , \qquad \left[\mathbf{I}+\Delta t\,\mathbf{D}_X\right]\Delta\mathbf{f}=\Delta\mathbf{f}^*\ , \tag{17}$$

where $\Delta\mathbf{f}^*=\left[\Delta u^*,\Delta v^*,\Delta p^*\right]^{\mathrm{T}}$ is a convenient intermediate variable vector.

These equations are further spatially discretized by central differencing on a stretched staggered grid, based on hyperbolic sine stretching functions in the X and Y directions (Mateescu *et al*. 1994a, b, 2001).

A special decoupling procedure, based on the utilization of the continuity equation, is then used for each sweep to reduce the resulting systems of discretized equations to two sets of decoupled scalar tridiagonal equations (for details on the decoupling procedure see Mateescu *et al*. (1994a, b, 2001).

3. METHOD VALIDATION FOR SYMMETRIC AIRFOILS

The method has been applied for validation to the flow at low Reynolds numbers past symmetric NACA airfoils at zero angle of attack. The computations have been performed using a stretched staggered grid with 257 × 181 grid points for each variable. The mesh spacing in the X-direction was minimum at the leading edge of the airfoil, $\Delta X_{\min} = 0.0007$, and maximum at the inflow and outflow boundaries, $\Delta X_{\max} = 1.06$, while in the Y-direction the minimum mesh spacing was at the walls (airfoil surfaces) $\Delta Y_{\min} = 0.0021$, and maximum at the upper or lower far-field boundaries, $\Delta Y_{\max} = 2.0$. Computations were performed on a computational domain defined by $L_0 = 10$, $L_1 = 10$, $H_1 = H_2 = 15$ with the value of the artificial compressibility taken as $\delta = 0.5$ and the pseudo-time step $\Delta t = 0.0005$; convergence was considered reached when all of the r. m. s. residuals were less than 10^{-5}, which corresponds to r. m. s. values of the delta quantities less than 10^{-9}. During the numerical procedure, the far field boundary conditions ($u=\cos\alpha$, $v=\sin\alpha$) on the upper and lower boundaries of the fixed rectangular domain are kept constant, which correspond to $\Delta u = 0$, $\Delta v = 0$ and $\Delta u^* = 0$, $\Delta v^* = 0$. A similar treatment is applied for the inflow boundary of the computational domain, while at the outflow the second order X-derivatives of the velocity components are imposed to be zero. The no-slip boundary condition, $u = 0$ and $v = 0$, is imposed on the airfoil surfaces.

The influence of the Reynolds number on the pressure coefficient distribution on symmetric airfoils at zero angle of attack is shown in Figure 2. One can notice a marked increase in the negative pressure coefficient on the airfoil with the decrease in the Reynolds number, which is due to a thicker boundary layer; this effect is more pronounced towards the trailing edge due to the boundary layer increase along the airfoil. At the same time, the variation of the pressure coefficient near the leading edge is smoother due to stronger viscous effects at smaller Reynolds numbers. The inviscid flow solutions (Mateescu & Abdo 2003, 2005), for $\mathrm{Re}\to\infty$, are also shown in Figure 2 for comparison, to indicate the dramatic change in the pressure distribution at low Reynolds numbers, which is even more pronounced for the thinner airfoil NACA 0002.

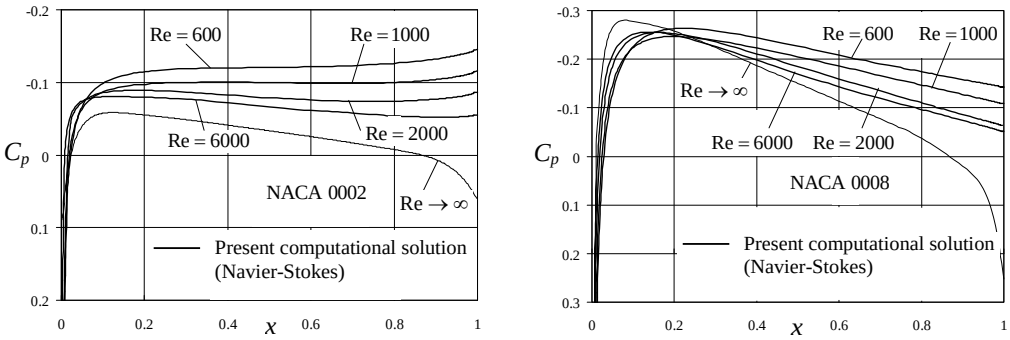

Figure 2. Influence of the Reynolds number on the pressure coefficient distribution on NACA 0002 and NACA 0008 airfoils at zero incidence

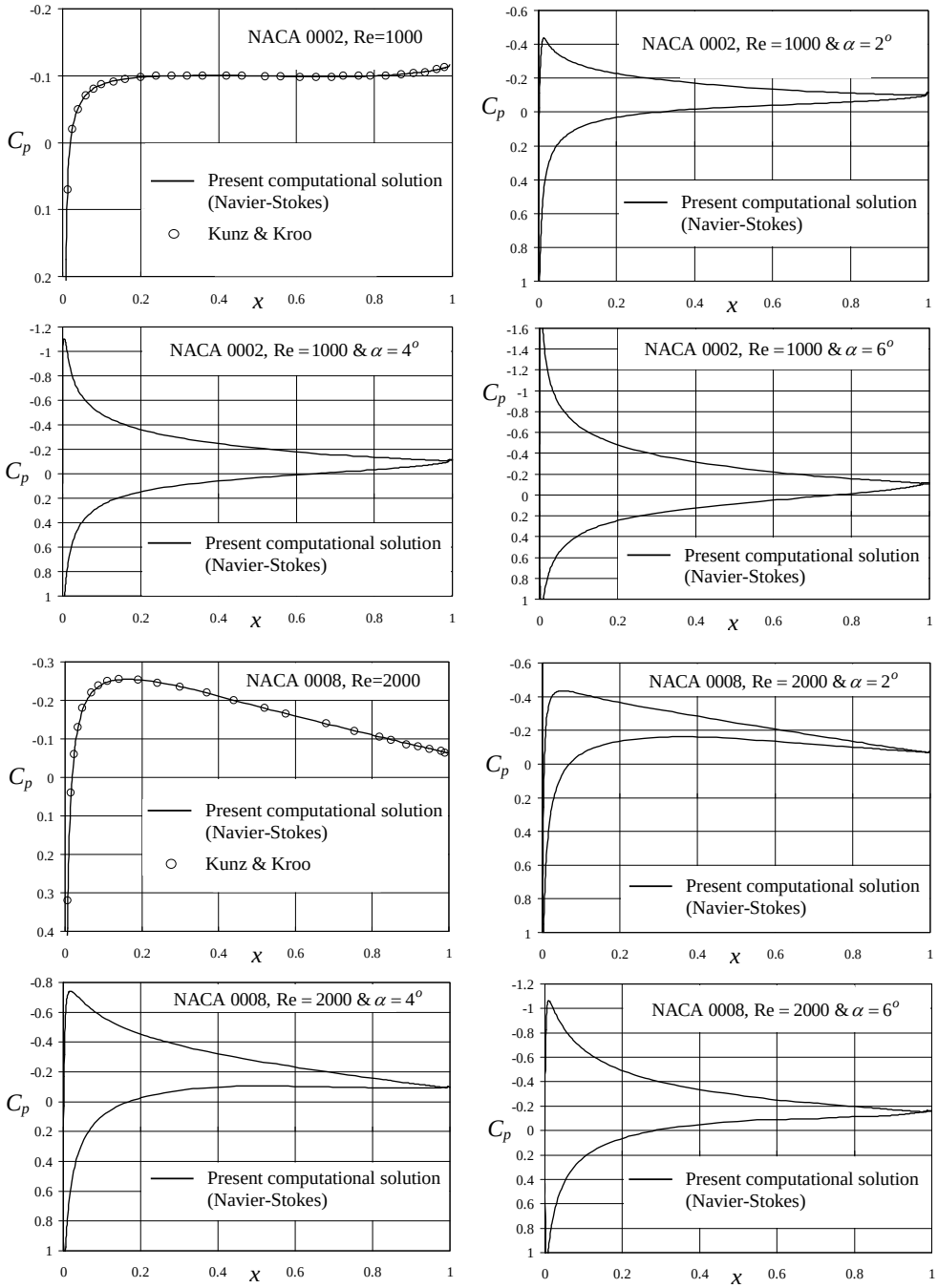

Figure 3. Pressure coefficient distributions on NACA 0002 and NACA 0008 airfoils at Reynolds numbers Re =1000 and 2000 and at angles of attack $\alpha = 0$, 2°, 4° and 6°

The present method has been validated by comparison with the results obtained by Kunz & Kroo (2000) using the INS2D code from NASA Ames (based on an upwind finite differencing scheme developed by Rogers & Kwak 1990), for two symmetric airfoils at zero angle of attack, NACA 0002 and NACA 0008, at three low Reynolds numbers: 1000, 2000 and 6000 (there are no previous results available for the pressure distribution on airfoils at incidence). The present solutions for the pressure coefficient distribution on these airfoils were found in excellent agreement with Kunz & Kroo results (2000), as shown in Figure 3 for Reynolds numbers 1000 and 2000.

4. SOLUTIONS FOR CAMBERED AIRFOILS AT INCIDENCE

Pressure coefficient distribution on various airfoils at incidence. Typical pressure coefficient distributions are presented in Figure 4 for two cambered airfoils, NACA 4402 and NACA 4404, of relative thickness 0.02 and 0.04, respectively, at several angles of attack and low Reynolds numbers. The effect of the relative thickness on the pressure coefficient distribution can be seen by comparing the results for the two airfoils in Figure 4.

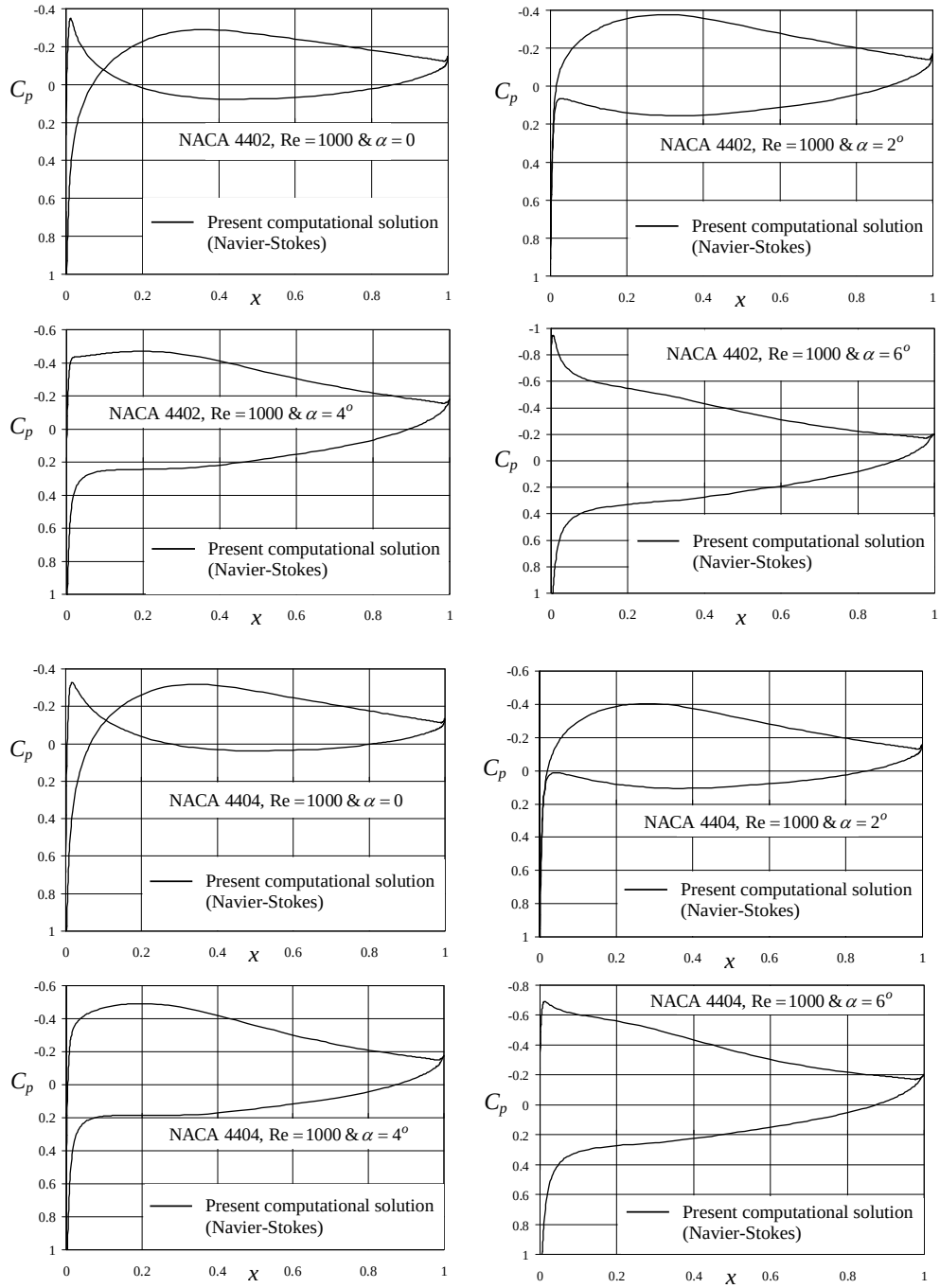

Figure 4. Pressure coefficient distribution on NACA 4402 and NACA 4404 airfoils at Reynolds number Re =1000 and at angles of attack $\alpha = 0$, 2°, 4° and 6°

Lift and drag coefficients. The variation of the lift and drag coefficients for the NACA 0002 and NACA 4402 airfoils are shown in Figure 5 for validation in comparison with previous results obtained by Kunz & Kroo (2000); one can notice a very good agreement between these results.

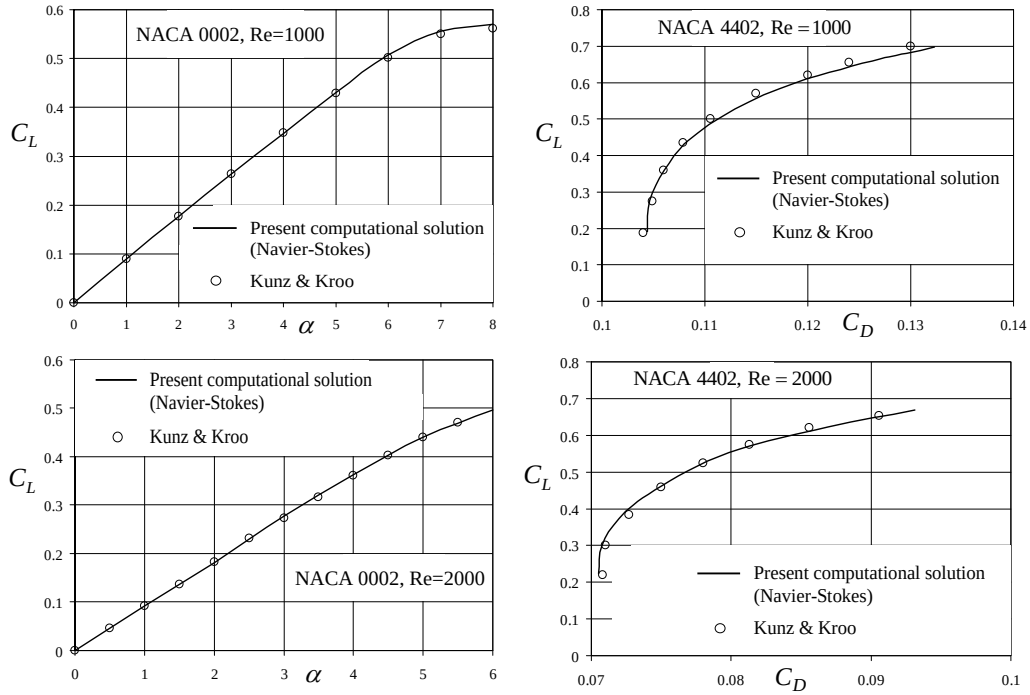

Figure 5. Lift and drag coefficients for NACA 0002 and NACA 4402 airfoils at two Reynolds numbers

Influence of low Reynolds numbers. The influence of the Reynolds number on the lift and drag coefficients is shown in Figure 6 for two cambered NACA airfoils, NACA 4404 and NACA 4702. One can notice that the drag coefficient is increasing with the Reynolds number, and the lift versus drag ratio is decreasing with the Reynolds number, especially at the large lift coefficients.

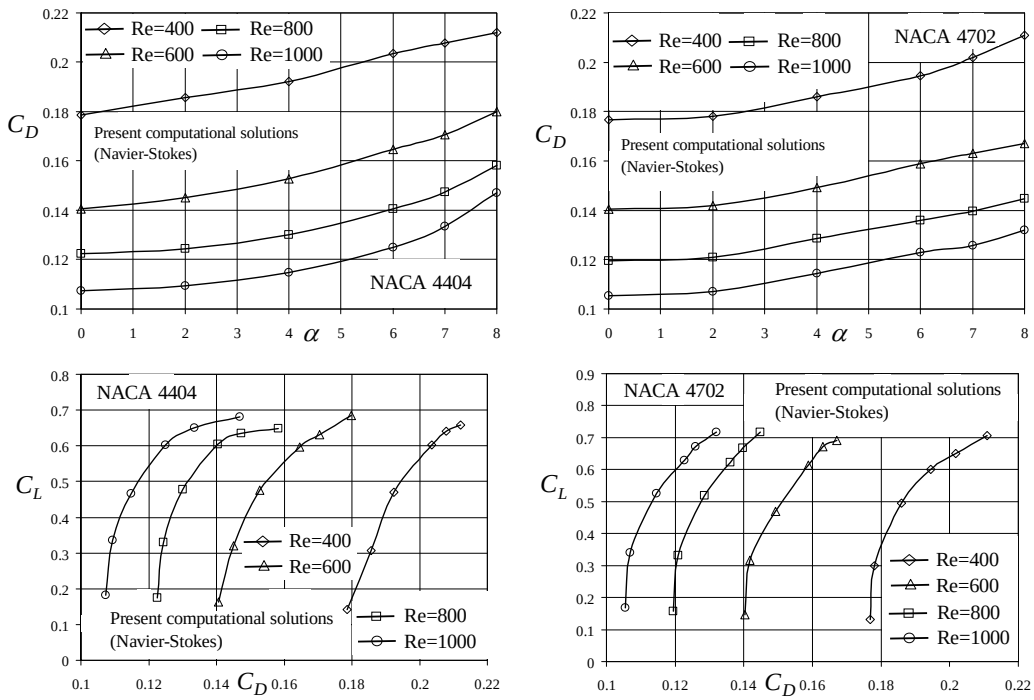

Figure 6. Influence of the Reynolds number on the lift and drag coefficients for NACA 4404 and NACA 4702 airfoils

Influence of the relative camber. The influence of the relative camber on the lift and drag coefficients is shown in Figure 7 for three NACA airfoils and Re=800. One can notice that both the lift and drag coefficients increase with the relative camber.

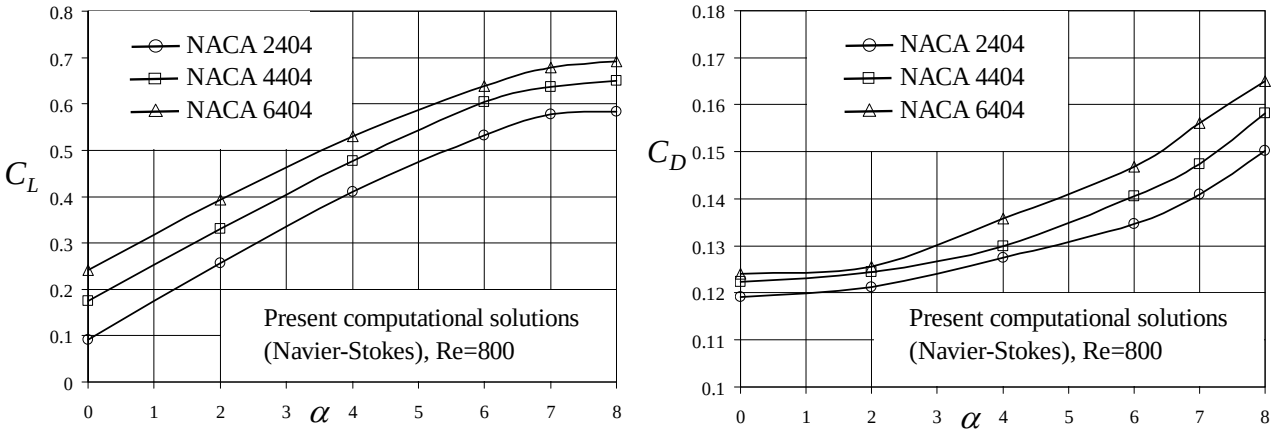

Figure 7. Influence of the airfoil camber on the lift and drag coefficients at Reynolds number 800

Influence of the relative thickness. The lift coefficient is increasing with the decrease in the relative thickness; this can be noticed from the pressure results illustrated in Figure 3 for two airfoil thicknesses (the lift results are not shown here due to space limitation).

5. STUDY OF THE FLOW SEPARATION ON AIRFOILS AT LOW REYNOLDS NUMBERS

At very low Reynolds numbers, the viscous effects in the flow become very important. As a result, the boundary layer developed on the airfoil contour become much thicker and flow separations may frequently occur at relatively smaller angles of attack at low Reynolds numbers. For this reason, a detailed study of the flow separations has been performed in this paper for airfoils at low Reynolds numbers. The positions x_s and x_r of the flow separation onset (defined by zero velocity gradient) and reattachment points on the upper surface of the airfoil, as well as the length of separation region, $l_s = x_r - x_s$, have been calculated and compared for four symmetric and nine cambered airfoils at various incidences and low Reynolds numbers. The main results obtained are presented in Tables 1 and 2. The streamline patterns of the flows past the same airfoils, which provide a better physical insight of the flow separations, have also been generated for these airfoils. Typical streamline contours for various airfoils, angles of attack and low Reynolds numbers are illustrated in Figure 8 for NACA 0004 airfoil at Reynolds number Re=2000 and three angles of attack.

Influence of the angle of attack. The influence of the angle of attack on the flow separation length $l_s = x_r - x_s$ is shown in Figure 8 for the symmetric airfoil NACA 0004 and in Table 2 for the cambered airfoil NACA 4404. One can notice that the flow separation length increases substantially with the increase in incidence, as the flow separation position is shifted closer to the leading edge. As shown in Figure 8 and Table 2, there is no flow separation at the lower Reynolds numbers when the angle of attack is smaller than 4°.

Influence of the Reynolds number. The Reynolds number has an important influence on the flow separation on the airfoils at incidence, as shown in Table 2. One can notice that the separation length is decreasing with the reduction in the Reynolds number, which can be attributed to the airfoil "*decambering*" due to relatively thicker boundary layers (on both sides of the airfoil) in the case of lower Reynolds numbers.

Influence of the relative thickness. The influence of the relative thickness on the flow separation is shown in Table 1 for four symmetric airfoils. One can notice a substantial increase of the flow separation length with the decrease in the relative thickness.

Influence of the relative camber and of the maximum camber position (results not shown due to space limitation). The flow separation length is increasing with the relative camber, as expected, and is substantially reduced by moving the maximum camber position towards the trailing edge (from 30% to 50% and further to 70%).

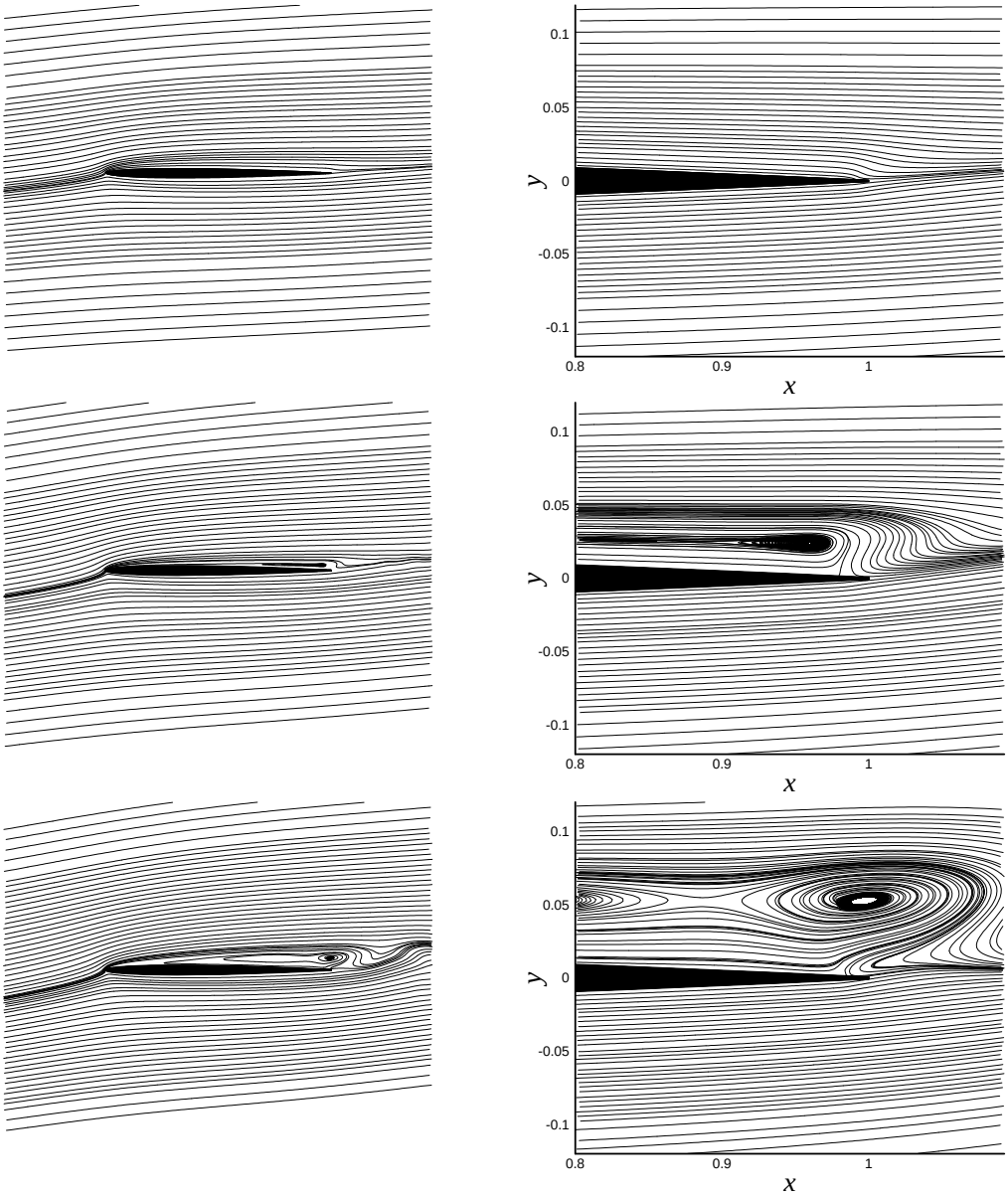

Figure 8. Streamline contours for NACA 0004 airfoil at Reynolds number Re=2000 and at $\alpha = 4^o$, 6° and 7°, respectively (an enlarged view of the trailing edge area is also shown for each incidence)

Table 1. Flow separation comparison for four symmetric NACA airfoils at Reynolds number Re=2000 and $\alpha = 6^o$.

Airfoil type	Separation position, x_s	Reattachment position, x_r	Separation length, l_s
NACA 0002	0.009448	0.983755	0.974307
NACA 0004	0.345298	0.985038	0.639739
NACA 0006	0.493517	0.987267	0.493749
NACA 0008	0.501505	0.986959	0.485453

Table 2. Comparison of the trailing edge flow separation for NACA 4404 airfoil at four Reynolds numbers and various angles of attack.

Reynolds number, Re		Re=400	Re=600	Re=800	Re=1000
$\alpha = 4^o$	x_s	No separation	No separation	No separation	0.901651
	x_r				0.978418
	l_s				0.076766
$\alpha = 6^o$	x_s	No separation	0.860459	0.777701	0.717352
	x_r		0.970041	0.976729	0.979368
	l_s		0.109581	0.199027	0.262016
$\alpha = 7^o$	x_s	0.894895	0.765829	0.682713	0.625532
	x_r	0.953618	0.971379	0.975893	0.977933
	l_s	0.058723	0.205550	0.293180	0.352401
$\alpha = 8^o$	x_s	0.800136	0.670082	0.592716	0.550572
	x_r	0.960186	0.969762	0.972774	0.975735
	l_s	0.160050	0.299680	0.380058	0.425163

6. ACKNOWLEDGEMENTS

The support of the Natural Sciences and Engineering Research Council of Canada is gratefully acknowledged, as well as the contribution of my former Ph.D. student, M. A. Abdo, to the numerical results presented in this paper.

7. SELECTED REFERENCES

Chorin, A. 1984 “A numerical method for solving incompressible viscous flow problems” Journal of Computational Physics, Vol. 2, pp. 12-26.

Kunz, P. and Kroo, L., 2000, “Analysis and design of airfoils for use at ultra-low Reynolds numbers”, Proceedings of the AIAA Fixed, flapping and rotating wing aerodynamics at very low Reynolds numbers conference, Notre Dame, June 5-7, pp. 35-60.

Lee,T. and Mateescu,D., 1998, “Experimental and numerical investigations of 2-D backward-facing step flow”, Journal of Fluids and Structures **12,** pp. 703-716.

Mateescu,D., Abdo,M.A., 2005, “Efficient second-order analytical solutions for airfoils in subsonic flow”, Aerospace Science and Technology Journal, Vol. 9, pp. 101-115.

Mateescu,D., Abdo,M.A., 2003, “Nonlinear theoretical solutions for airfoil aerodynamics”, 21st Applied Aerodynamics Conference, Orlando, Florida, AIAA Paper 2003-4296, pp. 1-22.

Mateescu,D. and Venditti,D.A., 2001, “Unsteady confined viscous flows with oscillating walls and multiple separation regions over a downstream-facing step”, Journal of Fluids and Structures, Vol. 15, pp. 1187-1205.

Mateescu,D., Païdoussis,M.P. and Bélanger,F., 1994a, “A time-integration method using artificial compressibility for unsteady viscous flows”, Journal of Sound and Vibration, Vol. 177, pp. 197-205.

Mateescu,D., Païdoussis,M.P. and Bélanger,F., 1994b, “Unsteady annular viscous flows between oscillating cylinders. Part I: Computational solutions based on a time integration method”, Journal of Fluids and Structures, Vol. 8, pp. 489-507.

Rogers,S. and Kwak,D., 1990 An upwind differencing scheme for the time-accurate incompressible Navier-Stokes equations, AIAA Journal 28, pp. 253-262.

8. RESPONSIBILITY NOTICE

The author is the only responsible for the printed material included in this paper.